

# Shaped Pupil Coronagraph: Disk Science Mask Experimental Verification and Testing

David Marx\*, Eric Cady, A. J. Eldorado Riggs, Camilo Prada, Brian Kern, Byoung-Joon Seo, and Fang Shi

Jet Propulsion Laboratory, California Institute of Technology, 4800 Oak Grove Drive, Pasadena, CA 91109

## ABSTRACT

The Shaped Pupil Coronagraph (SPC) is one of the two operating modes of the baseline coronagraph instrument for the proposed WFIRST mission. While in SPC mode, multiple sets of shaped pupil masks and focal plane masks would be available for various imaging tasks. The disk science mask set (SPC-DSM) is designed for exozodiacal disk science. With a 360 degree high contrast field of view, extending up to  $20 \lambda/D$ , the SPC-DSM provides a powerful tool to study exozodiacal dust clouds associated with stellar debris disks to gain insight of the exoplanet formation and stellar disk dynamics. We will describe the performance verification and demonstration of the SPC-DSM coronagraph as tested in the high contrast imaging testbed (HCIT) at JPL. The goal of the testbed demonstration is an average contrast of  $5e-9$  over a 10% bandwidth centered at 565nm, in a field of view extending from  $6.5 \lambda/D$  to  $20 \lambda/D$ . We will discuss electric field conjugation, performance metrics, and model agreement as applied to the SPC-DSM.

**Keywords:** Coronagraph, WFIRST,

## 1. INTRODUCTION

The Shaped Pupil Coronagraph (SPC) is one of the two operating modes of the baseline coronagraph instrument for the proposed WFIRST mission. While in SPC mode, multiple sets of shaped pupil masks and focal plane masks would be available for various imaging tasks. The disk science mask set (SPC-DSM) is designed for exozodiacal disk science—debris disks, densities, morphologies, and planetary systems.

Last year, Riggs presented a mask design for the SPC-DSM [1], and here we present results of the testbed implementing the fabricated mask. The testbed was assembled and placed inside a vacuum chamber at the JPL high contrast imaging testbed (HCIT) facility. The primary goal of the testbed demonstration was to achieve  $5e-9$  mean contrast over an annular field of view (FOV), from  $6.5 \lambda/D$  to  $20.0 \lambda/D$ , and a 10% wavelength band centered at 565nm. To achieve this goal, the electric field conjugation (EFC) optimization algorithm was used, along with pair-wise probes to estimate the electric field in the image plane [4]. After achieving high contrast, a second goal for the testbed was to measure the sensitivity of mean contrast to wavefront errors.

The testbed effort achieved both goals, with a best mean broadband contrast of  $3.5e-9$ . With an outer working angle of  $20.0 \lambda/D$ , this coronagraph has a significantly wider FOV than previous coronagraphs demonstrated in the HCIT. For example, the hybrid Lyot coronagraph [2] and the other shaped pupil coronagraph [3] each had a FOV of  $3 \lambda/D$  to  $9 \lambda/D$ . The wide FOV of the SPC-DSM testbed required better knowledge of the influence functions of the deformable mirrors for EFC performance, because the modulation of the field at outer working angles rolls off with the transform of the influence function.

In Section 2, we describe the testbed and the results of EFC, best contrast, and sensitivity to wavefront error. In Section 3, we explain the considerations of influence function knowledge and pair-wise probing due to the wide FOV.

\*David.S.Marx@jpl.nasa.gov; phone 1 818 354-2837

## 2. SHAPED PUPIL DISK SCIENCE CORONAGRAPH TESTBED

The SPC disk science testbed was essentially the same testbed as the shaped pupil testbed previously reported [1], but with the shaped pupil mask, focal plane mask (FPM), and Lyot mask replaced.

The layout of the testbed is shown in figure 1a, and an image of the shaped pupil mask is shown in figure 1b. The coronagraph includes two deformable mirrors (DM). The pupil diameter is 46.3mm. The Lyot stop inner diameter is 26% and outer diameter is 88%. The off-axis parabolic (OAP) mirror that forms the final source image, OAP6, is positioned non-telecentric so that an image of the pupil occurs about 200mm after the source image. The camera is on a stage with about 250mm of axial travel so that images of the source, pupil, and defocused source and pupil, can be recorded and used for phase retrieval.

Before the start of electric field conjugation (EFC) to form the high contrast image, we use DM1 to make the pupil phase flat. Phase retrieval with the FPM and Lyot masks removed measured the pupil phase, and after a few iterations of adjusting DM1 and measuring pupil phase, the pupil phase was below  $\text{mrad}$ . The shaped pupil mask has significant astigmatism, and so after flattening the pupil phase, DM1 was primarily shaped to the negative astigmatism.

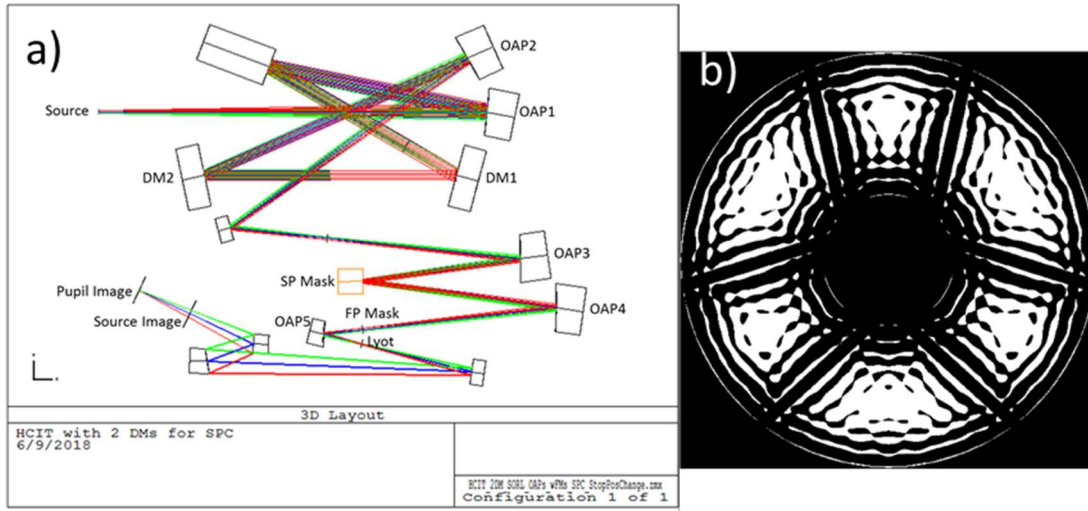


Figure 1. a) Optical layout of the coronagraph testbed. b) The shaped pupil mask design for the WFIRST pupil. The mask was fabricated in “black” silicon.

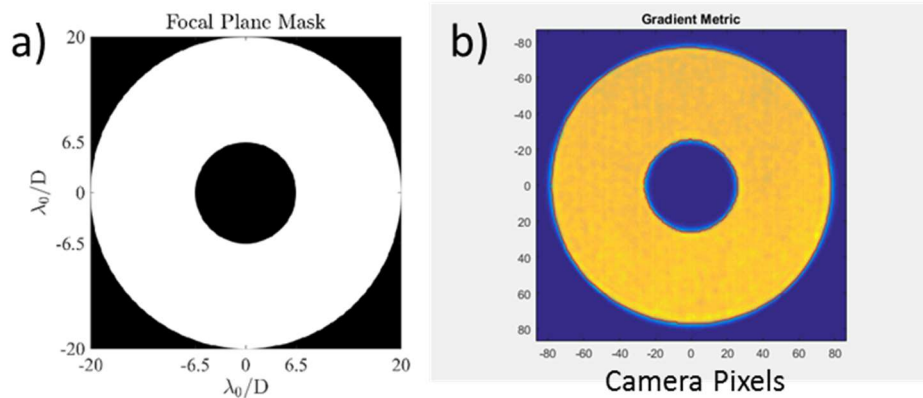


Figure 2. Focal plane mask a) design and b) as imaged in the testbed. The image was formed by placing a diffuser after the source, and this FPM image was used to find the best focus position of the FPM.

To build the control model used to calculate the Jacobian as part of EFC, pupil amplitude and phase, images of the FPM, shaped pupil mask, and Lyot stop were recorded and incorporated into the control model. EFC started with the testbed in the state of best flat pupil phase. Figure 3 shows the convergence of normalized intensity in the FOV as EFC iterated. Interruptions to the EFC iterations included drift measurements (iterations #42 to #52), and photometry measurement after iteration #240. For most of the EFC iterations, only three 2% wavelength bands, centered at 542.4nm, 565.0nm, and 587.6nm were used for control to reduce the time per iteration. Prior experience has shown that EFC convergence is not significantly affected by using only three wavelength rather than all five that cover the 10% spectrum. After the high contrast was achieved, we re-measured photometry and continued EFC iterations using all five wavelength bands so that we could make a valid measurement of contrast across the full band.

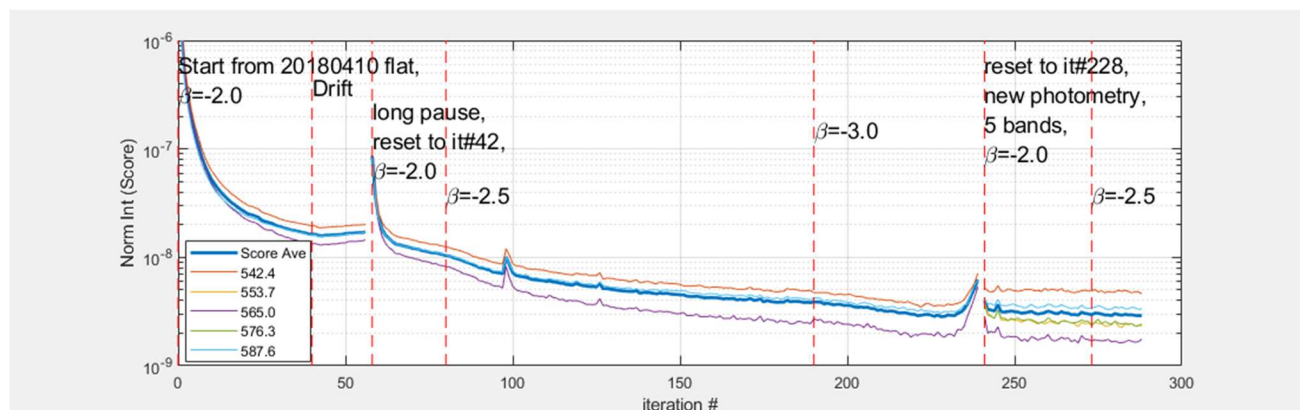


Figure 3.  $\beta$  is the regularization parameter.

The contrast at each wavelength and for different parts of the FOV is shown in a table in figure 4. Mean contrast for the entire FOV was  $3.49\text{e-}9$ , limited by light and throughput at the inner and outer working angles. Because of the edged on the FPM block light at the inner and outer working angles, PSF throughput falls at those angles, thereby reducing contrast. As shown in the radial plot in figure 5a, the short wavelength band, 542nm, is the brightest band at both the inner and outer working angles, implying that this band was more difficult for EFC than the other bands. This result is unexpected, as the more typical result would be that the short wavelength is more difficult to control at the outer edge, but the long wavelength would be more difficult to control at the inner edge. One possible explanation is control model knowledge error, which is discussed below.

A further indication of the difficulty of controlling the light at the outer working angle is the presence of unmodulated light in that part of the FOV (figure 5b). Unmodulated light was insignificant throughout EFC for most of the FOV. The presence of unmodulated light concentrated at the outer FOV indicates error in electric field estimation from the pairwise probing. Probe amplitude images are shown in figure 8, and are discussed further below.

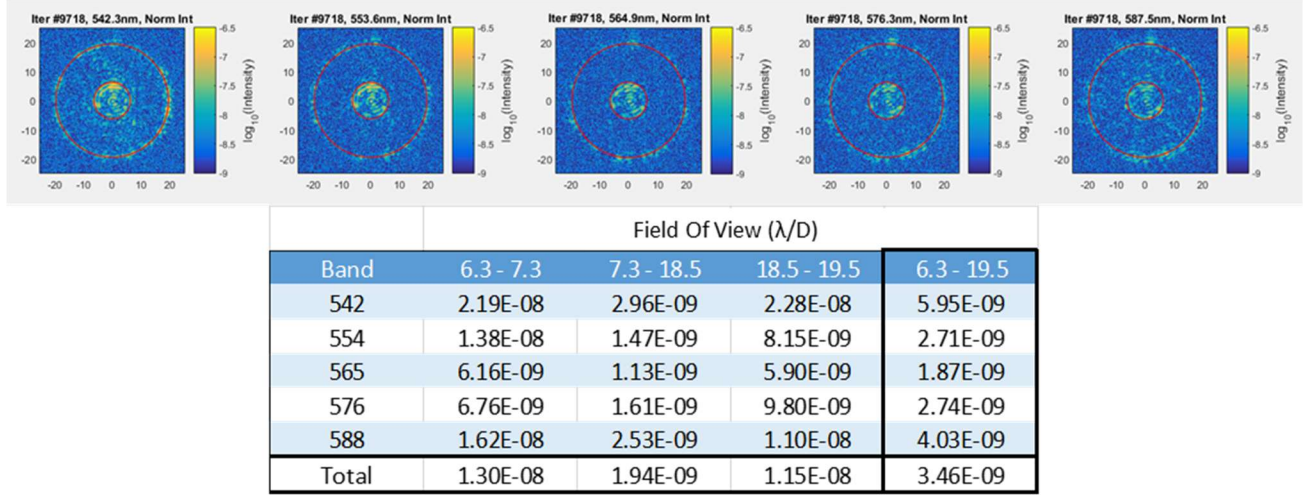


Figure 4. Normalized intensity images and tabulated contrast for wavelength and FOV.

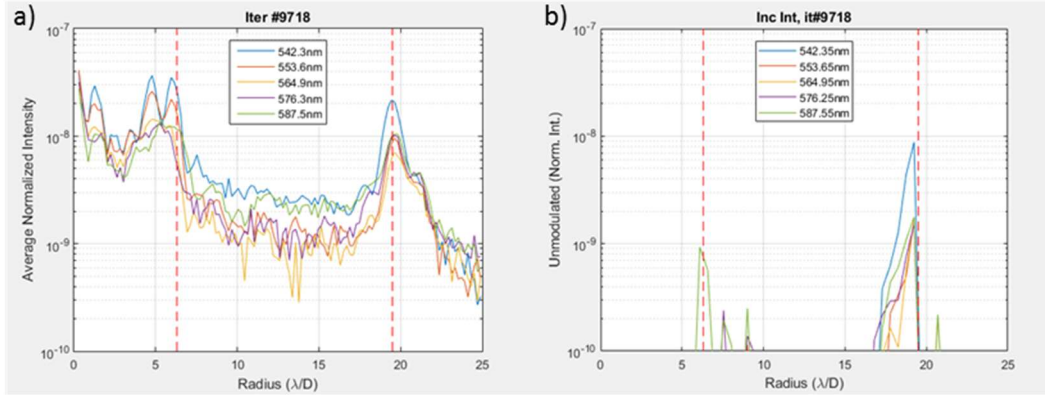


Figure 5. Radial plots of a) mean normalized intensity, and b) unmodulated component of the normalized intensity, at the coronagraph's best contrast. The unmodulated intensity at the best iteration is insignificant, except for the short wavelength at the outer working angle.

Having achieved the contrast goal for the testbed, the second task was to measure the sensitivity of contrast to wavefront error (WFE). Because the inner working angle of  $6.3 \lambda/D$  is large compared to the previous coronagraph tested in the HCIT, we expect the SPC-DSM coronagraph to be less sensitive to WFE than the previous coronagraphs. Typically, WFE sensitivity of the normalized intensity in the FOV to WFE has been measured by using one of the DM's to create WFE's, one Zernike mode at a time and of varying magnitude, and then recording the change in the source image. When deforming the DM to a specific Zernike mode, the deformation always includes some error that is the difference between the desired WFE and the actual mirror deformation. The error is due to several factors such as actuator gain errors, influence function variations, and alignment registrations. Furthermore, these errors are approximately white in spatial frequency thereby affecting the normalized intensity across the FOV. In the case of the SPC-DSM coronagraph, the change in average normalized intensity due to these DM deformation errors was about two orders of magnitude greater than the change expected from a pure low order Zernike mode. To test the effect of the deformation error, we applied a Zernike mode to DM1, and the negative of the same mode to DM2. If there were no deformation error, then the result would have been a small total WFE and little change to the image normalized intensity. However, the result we saw was an increase in normalized intensity of about  $\sqrt{2}$  beyond the increase in normalized intensity when the Zernike mode WFE was applied to only one DM. The conclusion is that the coronagraph's sensitivity to WFE is smaller than can be measured by applying low order WFE's to the DM.

Tip/tilt WFE (Zernike modes 2 and 3) were measured by translating the FPM. For this testbed,  $0.14\mu\text{m}$  translation of the FPM corresponds to 1nm rms tip/tilt. To obtain measurable changes in the mean normalized intensity, we had to translate the FPM to create several nm of rms tip/tilt.

Defocus WFE (Zernike mode 4) was created in the testbed by mechanically defocusing the source relative to the first OAP. The rate of defocus was about  $8.7\mu\text{m}$  axial displacement per 1nm rms WFE. Again, we had to impose several nm rms WFE to create a measureable change in the mean normalized intensity.

Figure 6 plots the change in the mean normalized intensity in the FOV per 1nm rms WFE for various Zernike modes. As described above, only Zernike modes 2, 3, and 4 could be measured. Also plotted are the sensitivities predicted numerically by the control model. For a fair comparison between modeled and measured sensitivities, the contrast state of the numerical model should be similar to that of the testbed. For the results shown in the figure, the mean normalized intensity in the FOV for the model is about  $2.0\text{e-}9$ .

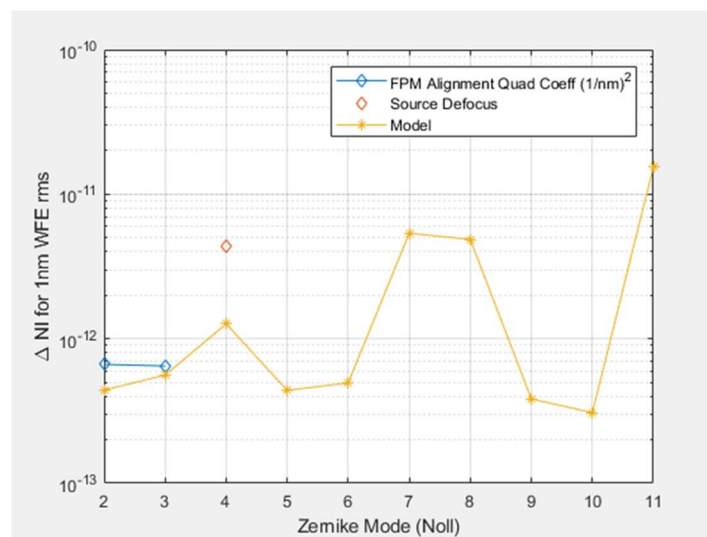


Figure 6. WFE sensitivity of the mean normalized intensity in the FOV comparing measurement to the control model. Only tip, tilt, and defocus could be measured by the testbed.

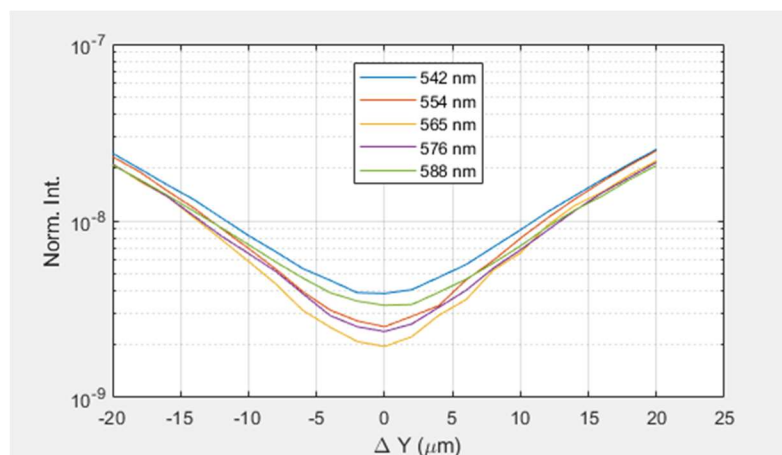


Figure 7. Sensitivity to shaped pupil mask movement,  $5\text{e-}11 \Delta\text{NI} / \mu\text{m}^2$



### 3. EFFECT OF WIDE FOV ON EFC

The large outer working angle of the FOV introduced considerations that were not significant in other coronagraphs tested in the HCIT, where the outer working angle did not go beyond  $10 \lambda/D$ . One such consideration is the falloff of the probe amplitude with working angle. To understand why the probe amplitude falls off with FOV angle, consider the probe as a modulation of the pupil field formed by the convolution of the actuator pattern with the influence function. Then probe amplitude in the FOV is approximately equal to the Fourier transform of the probe's actuator pattern multiplied by the Fourier transform of the influence function. Thus, the amplitude of the Fourier transform of the influence function forms an amplitude envelope across the FOV. Figure 8 shows the probe amplitudes of the six probe patterns used in EFC, and the cross-section for the second probe. From the cross-section plot (figure 8b), the probe amplitude at the outer working angle is approximately one-tenth the maximum amplitude near the inner working angle. In general, the reduced probe amplitude is not a significant problem unless it falls below the read noise limit. For this testbed, the probe amplitude at the outer working angle, though reduced, was still sufficient for EFC.

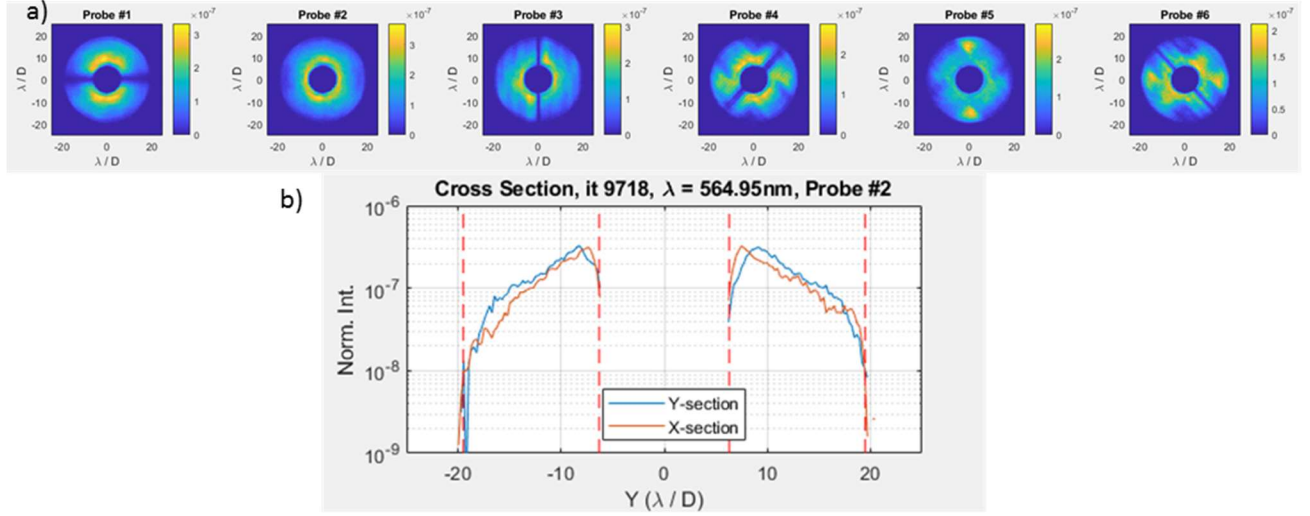


Figure 8. a) Probe amplitude across the FOV for six probe pairs. b) cross-section of probe amplitude for probe #2, the “even” probe.

However, the effect of the amplitude envelope formed by the Fourier transform of the influence function increases the sensitivity of EFC to knowledge error of the influence function itself. As an example, consider the transfer function (amplitude as a function of spatial frequency or FOV) for two different influence functions, figure 9. Each of these influence functions has been used in the control model for EFC for coronagraphs in the HCIT. If the real, physical, influence function in the DM in the testbed were accurate to “inf 64”, for example, but the influence function “inf 48” were used in the control model for EFC, then the Jacobian computed as part of EFC will underestimate the electric field modulation at the higher spatial frequencies. The result is poor EFC performance. In particular, the relative error, shown in figure 9c, is significantly worse at the higher spatial frequencies. Therefore, this effect of influence function “knowledge error” has a worse effect on EFC for this SPC-DSM coronagraph than for other coronagraphs where the outer working angle is  $< 10\lambda/D$ .

To experimentally test the accuracy of the control model prediction of the actuator transfer function, we recorded pupil images while modulating one actuator 50mrad in the positive and negative directions. Since the FPM acts as a bandpass filter, transmitting only spatial frequencies between 6.3 and  $19.5 \lambda/D$ , the mean intensity of light in the Lyot plane is a measure of the influence function transfer function at those spatial frequencies. Specifically, the metric for actuator (i,j) is:

$$M_{i,j} = \sum_{FOV} [0.5(I_+ + I_-) - I_0],$$

where  $I_0$  is the pupil intensity with no actuator modulation. Figure 10 plots the modulation metric for each actuator in DM2, comparing testbed measurement to values predicted by the control model. The third plot displays the log of the ratio of the metric, and the ratio indicates that the testbed modulation is stronger than predicted by the control model similar to the relative intensity in the FOV shown in figure 9c.

The EFC convergence and best contrast result shown above were obtained after replacing the influence function in the control model from “inf 48” to “inf 64”, providing a final validation of this transfer function effect.

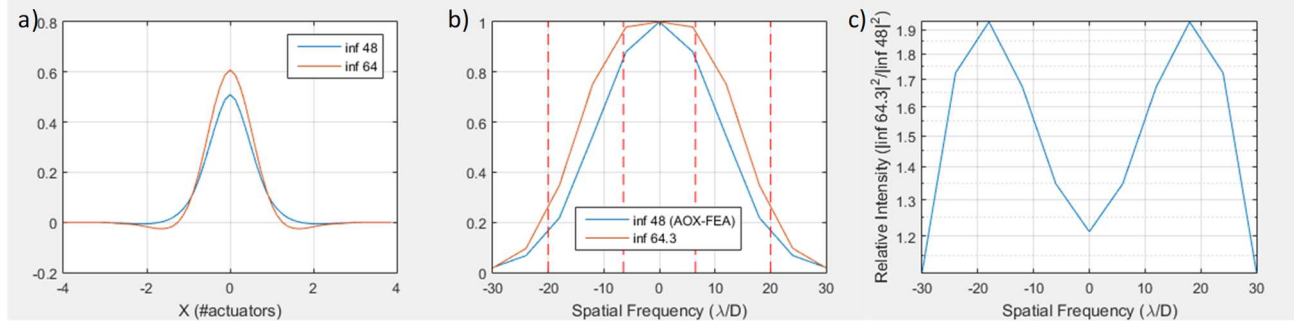


Figure 9. Effect of influence function shape on modulation near the outer FOV working angles.

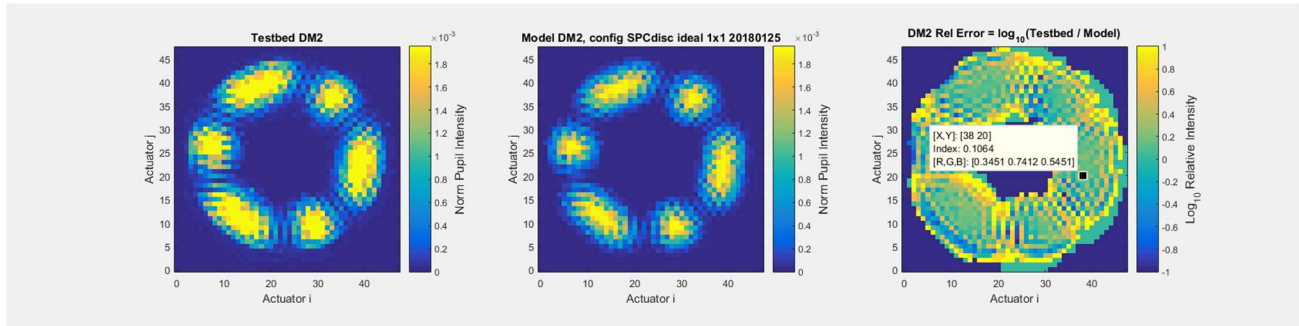


Figure 10. Normalized pupil intensity in the Lyot plane when actuator ( $i,j$ ) is displaced 3mrad

Measure influence function: create speckles for each working angle; white noise added to DM; delta function (single actuator) modulation.

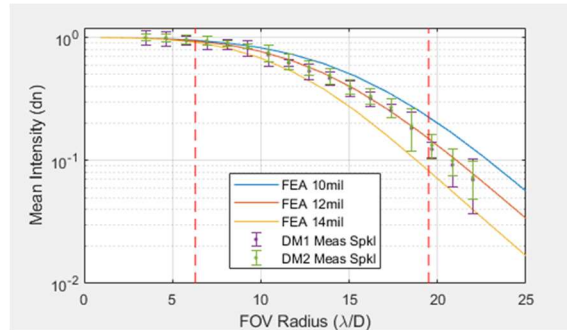


Figure 11. Direct measurement of the influence function agrees with the calculated influence function for the 12mil thick facesheet.

Plate scale error is another effect that increases at large FOV angles. It is measured by applying a sinusoid modulation at DM1, and recording the pixel separation of the resulting speckles in the image plane. The measured plate scale for this SPC-DSM testbed was 4.01 pixels / ( $\lambda/D$ ). Referring back to the radial plot of normalized intensity versus wavelength, figure 5a, and comparing to the prediction from the control model when at a similar contrast state, figure 13c, we notice the lack of agreement for the short wavelength, 542nm, at the outer working angle. To test whether this worse than expected

performance of the testbed at the outer working angle might be due to plate scale error, we used a “knowledge mismatch model” to reproduce the effect.

The schematic in figure 12 represents the plate scale error simulation. The “test model” represents the testbed and uses a plate scale equal to the nominal value plus an error. The “EFC Model” is exactly the EFC routine containing the identical control model as used for the testbed. In contrast to the real testbed, this simulation does not include probing so that probe errors are eliminated from the test, and plate scale is the only error that can cause a difference between the “test model” and the “EFC model”. For each iteration, the “test model” calculates the electric field in the image plane, and then EFC performs the usual computation using the control model to calculate the Jacobian and the change in DM values to cancel the electric field. The new DM values are sent to the “test model”, and the next iteration proceeds.

Results of the simulation for different plate scale errors are shown in figure 13. Comparing the intensity of the short wavelength at the outer working angle to the testbed result, a plate scale error of 0.5% (3.99 to 4.01 pixels / ( $\lambda/D$ )) gives a good fit.

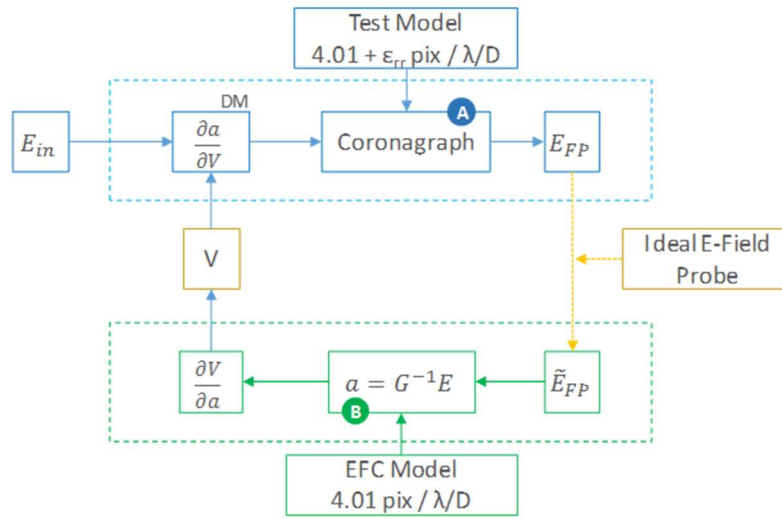


Figure 12. Schematic of the numerical model to evaluate EFC performance in the presence of control model “knowledge errors”, such as plate scale error.

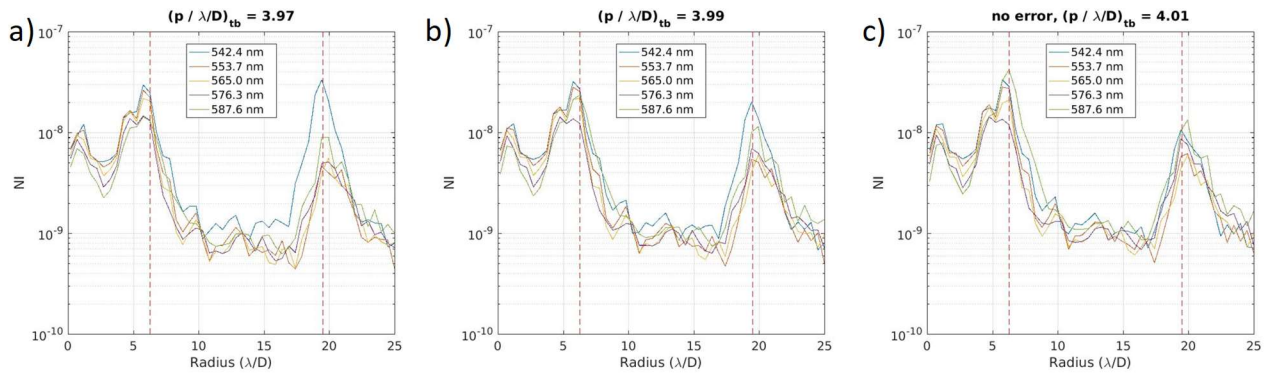


Figure 13. Effect of plate scale error on the spectrum of the excess light at the outer working angle.



## 4. CONCLUSIONS

The SPC-DSM testbed demonstration was a success, achieving mean contrast of  $3.5\text{e-}9$  over a measured annular FOV of 6.3 to 19.5  $\lambda/D$ , and 10% wavelength range. The sensitivity of contrast in the FOV to tip, tilt, and defocus was small, but measureable, at about  $7\text{e-}13 \Delta\text{NI} / \text{nm}^2$  rms tip and tilt, and about  $5\text{e-}12 \Delta\text{NI} / \text{nm}^2$  rms defocus. The sensitivity to higher order errors was not measureable because DM shape error dominated over the Zernike wavefront error. Challenges for efficient EFC optimization for the testbed were created by the wide FOV. For example, the probe amplitude at the outer working angle was weak, and improved knowledge of the influence function for the control model was required. The effort included direct measurement of the influence function for each DM. Finally, we found that plate scale error affected EFC performance of the short wavelength band at the outer working angle, and this effect was verified through numerical modeling.

## ACKNOWLEDGEMENT

The research was carried out at the Jet Propulsion Laboratory, California Institute of Technology, under a contract with the National Aeronautics and Space Administration. The decision to implement the WFIRST mission will not be finalized until NASA's completion of the National Environmental Policy Act (NEPA) process. This document is being made available for information purposes only.

## REFERENCES

- [1] Riggs, A. J. Eldorado, Zimmerman, N. T., Nemati, B., and Krist, J., "Shaped pupil coronagraph design improvements for the WFIRST Coronagraph Instrument," Proc. SPIE 10400, (2017).
- [2] Seo, B., Cady, E. J., Gordon, B., Kern, B. D., Marx, D. S., Moody, D., Muller, R., Patterson, K., Poberezhskiy, I., Shi, F., Sidick, E., Trauger, J. and Wilson, D., "Hybrid Lyot coronagraph for WFIRST: high-contrast broadband testbed demonstration," Proc. SPIE 10400, 10400-15 (2017).
- [3] Cady, E. J., Kunjithapatham, B., Gersh-Range, J., Kasdin, J., Kern, B. D., Lam, R., Prada, C. M., Moody, D., Patterson, K., Poberezhskiy, I., Riggs, A. J. E., Seo, B., Shi, F., Tang, H., Trauger, J., Zhou, H., Zimmerman, N. T., "Shaped pupil coronagraphy for WFIRST: high-contrast broadband testbed demonstration," Proc. SPIE 10400-14 (2017).
- [4] Give'on, A., Kern, B. K., and Shaklan, S., "Pair-wise, deformable mirror, image plane-based diversity electric field estimation for high contrast coronagraphy," Proc. SPIE 8151, 815110-01-10 (2011).